

Elastic compliances and stiffnesses of the fcc Lennard-Jones solid

D. J. Quesnel

Department of Mechanical Engineering, University of Rochester, Rochester, New York 14627

D. S. Rimai and L. P. DeMejo

Office Imaging Research and Technology Development, Eastman Kodak Company, Rochester, New York 14650

(Received 11 December 1992; revised manuscript received 2 June 1993)

The isothermal elastic compliances, stiffnesses, and bulk moduli of a Lennard-Jones solid organized into an fcc crystal structure (256 atoms in 4^3 unit cells) have been calculated as a function of testing temperature (expressed as the mean kinetic energy per atom). Tests conducted in pure shear were used to determine S_{44} and $C_{44} = G_{100}$, where 100 refers to crystallographic directions. Tests imposing axial elongation with fixed lateral dimensions established C_{11} and C_{12} . Axial deformation with zero lateral pressure (a tension test) was used to determine S_{11} , S_{12} , E_{100} and ν_{100} . This provided an independent set of results for comparison with the dilatational stiffnesses C_{11} and C_{12} . The bulk modulus K was obtained by independent triaxial tension testing. The stiffnesses, compliances, and moduli were determined by regression analysis and digital filtering applied to combinations of the stress-tensor and strain-tensor data stored at each iteration during the constant-rate deformation experiments. While the cubic fcc Lennard-Jones solid expectedly obeys the Cauchy relations for central-force potentials, it is not isotropic, allowing ν to take on values other than $\frac{1}{4}$ as originally proposed by Poisson. The present calculations show $\nu_{100} = 0.347$ for the fcc Lennard-Jones solid with a Young's modulus of $E_{100} = 61.1\epsilon/\sigma^3$, an initial (as indicated by superscript 0) shear modulus of $G_{100}^0 = 57.2\epsilon/\sigma^3$, and an initial bulk modulus of $K^0 = 71.2\epsilon/\sigma^3$ at zero temperature. The moduli all decreased with increasing temperature. Reuss, Voigt, and Hashin and Shtrikman [J. Mech. Phys. Solids **10**, 335 (1962)] bounds on the isotropic elastic properties of polycrystalline aggregates of Lennard-Jones material were also determined. Computed values of the moduli are in reasonable agreement with experimental results for solid argon and crystalline polyethylene.

I. INTRODUCTION

The trend in molecular-dynamics modeling has been to tailor interatomic potentials to produce close matches between the physical properties of the real system and the model system.¹ In this way the models should gain predictive power with respect to those physical properties that are not directly included by adjustment of the potentials.

On the other hand, certain potentials have been used historically to represent the behavior of physical systems. Potentials such as the Lennard-Jones potential are elegant in their simplicity, capturing the essence, if not the specific detail, of interatomic interactions. This simple potential is still widely used to represent the behavior of solids and liquids,²⁻⁶ particularly in the area of modeling of polymeric materials.⁷⁻⁹ Here, effective Lennard-Jones parameters are determined by empirical means from polarizability and molar diamagnetic susceptibility^{10,11} and then used to model other properties of the systems. It is important for researchers to know the properties that are produced as a consequence of modeling their system by a simple potential. These properties can then be compared with the measured elastic properties tabulated in compilations such as Simmonds and Wang¹² and the measured thermodynamic properties tabulated in references such as Touloukian.¹³ In addition, recent analytical attention has been devoted to examining and

modeling fundamental elastic behaviors of solids in both single^{1,2} and polycrystalline³ forms.

In this paper we report the results of computer experiments that simulate the measurement of isothermal single-crystal elastic constants of the fcc Lennard-Jones solid. Since the Lennard-Jones potential is so often used to represent the properties of solids ranging from solid argon^{5,6,14} to complex polymers^{7,9} it is important to document the elastic properties, the thermodynamic properties, and the relationships between them that are direct results of assuming the Lennard-Jones potential. This paper focuses on the elastic properties of the fcc Lennard-Jones solid.

II. COMPUTATIONAL METHODOLOGY

The computational methodology employed in this work has been modeled after experimental procedures used to measure the elastic properties of solids. The various program segments used in the computations are outlined briefly with detailed descriptions of the underlying algorithms published separately.¹⁵ In this section experimental steps are described for designing the test specimens and allowing the system to equilibrate to a given temperature and pressure in order to obtain the desired material properties. Once the specimens were ready, a constant rate of deformation to a predetermined strain was applied in one of several modes. The stress- and

strain-tensor data were recorded during the test. Following each deformation, the data were examined and the appropriate information stored for subsequent evaluation as described in the results section.

A. Specimen preparation

Specimens were made by positioning atoms on simple cubic lattice sites subject to the constraint that the indices describing the location of the site sum to an even number.¹⁶ This produced an fcc array with an atom at the origin. The initial lattice parameter was selected to minimize the potential energy of the system in this configuration. Velocity components of each atom were selected by a seeded random number generator and transformed¹⁷ to provide a Maxwell-Boltzmann distribution of initial velocities. The initial velocities were implemented by adjusting the prior positions of the atoms to reflect their intended velocities.

Atoms were then released and allowed to interact through the Lennard-Jones potential,

$$\phi = -4\epsilon \left[\left(\frac{\sigma}{r} \right)^6 - \left(\frac{\sigma}{r} \right)^{12} \right], \quad (1)$$

where ϵ represents the binding energy between one atom and its neighbor and σ represents the spacing between atoms where the potential crosses zero. These two parameters, along with the atomic mass m then become the fundamental units in which all other parameters are expressed. In this way, calculations can be performed without reference to values of the fundamental units. For example, the temperature of the system can be expressed as the average kinetic energy per atom, measured in units of ϵ , whereas the pressure, and hence the elastic moduli, are expressed in units of ϵ/σ^3 . Numerical values in SI units for quantities calculated using the Lennard-Jones potential can be obtained directly from a knowledge of the values of the fundamental units. Lennard-Jones parameters for a number of polymer systems are tabulated in Ref. 10.

When the atoms are first released, the system is not at equilibrium. Rather, all the system energy is in the form of kinetic energy, which rapidly equipartitions into an equal mixture of kinetic and potential energies during the first 50 iterations. Because this results in an approximately 50% decrease in the kinetic energy per atom, the initial velocities were made proportionally larger so that the kinetic energy per atom after the equipartitioning is approximately correct.

B. Algorithm implementation

Newton's laws are integrated on each iteration using the Verlet algorithm.^{5,6,18} The development of this simple, stable, and widely used third-order finite difference method from two Taylor-series expansions is given in detail in a recent text on molecular simulation.¹⁸ The dimensionless time increment of $0.01\sigma\sqrt{m/\epsilon}$ used throughout this work was sufficiently small so as to allow the energy of the system to remain approximately constant over several thousand iterations. Periodic boundary

conditions were established by assuming that atoms existed at each of the 27 locations obtained by permuting the X , Y , and Z dimensions of the computational box which contains the 256 atoms of the present calculation.

The locations of the atoms at the present, past, and future time steps were maintained in arrays allowing the future locations to become the present locations and the present locations to become the past locations merely by changing an index that references the temporal state of the data. This temporal rollover eliminated the need to copy data into fixed arrays for the purpose of implementing the motions. The interatomic force law, namely the derivative of the potential function, was then implemented as a look-up table and calculated once at the beginning of the program. Special features of the interaction force function could then be implemented without adding computation time into each iteration. A look-up list of a given atom's nearest neighbors was also implemented, dramatically increasing the execution speed and eliminating problems associated with changes in the dimensions of the lattice during straining and its effects on the cutoff radius. A cutoff radius of 3σ was used in all the calculations presented in the current paper. The initial size of the computational box was 6.349σ , producing no overlap of the regions of influence of a given atom with its periodic images, even during the compressional deformations that occurred as a result of Poisson contraction during a tension test.

C. Temperature and pressure controllers

Once the system of 256 atoms had equipartitioned and established a well defined pressure on the walls of the periodic boundary container due to the thermal expansion associated with the approximately correct temperature, subroutines that control temperature and pressure were activated. These temperature and pressure controller routines started at 100 iterations and continued until 1000 iterations when the various deformation routines were activated. The temperature and pressure controllers could be turned off during testing, thereby allowing for constant volume and/or adiabatic conditions during the deformation. Tests were conducted with each permutation of the active states of the temperature and pressure controllers. These controllers use causal digital filtering^{17,19} to temporally average temperatures and pressures, thereby producing relatively smooth measured numerical signals which represent the current values of the temperature and pressure. The measured signal was compared to a command signal, after which, the velocities of the atoms or the dimensions of the computational box were scaled to make the measured signals approach the command signals. These closed-loop feedbacks simulated the closed-loop feedback methodology used in experimental setups. Pressure was equated to the negative bulk stress using the stress-tensor data discussed below. These controllers have different gains in their feedback loops, operationally giving them different time constants for their response to step inputs. In this way, the temperature controller, with a time constant of about 10 iterations, does not influence the pressure controller, which

has a time constant of about 50 iterations. If both controllers are run with the same time constants, temperature changes influence the pressure of the system and lead to unstable behavior.

D. Constant-rate deformation

Constant-rate deformation was implemented by changing the dimensions of the computational box. On each iteration of a tensile test for example, the X dimension of the computational box was incremented by an engineering strain of 2×10^{-6} . When performing this deformation, the positions of all the atoms were moved photographically, i.e., in direct proportion to the numerical value of their spatial coordinates, in order to suppress the development of sound waves that would result by only moving the ends of the box. The pressure controller, when implemented, was switched to respond only to pressures on the two free sides of the specimen. In this way, the free sides of the sample could move inward to produce the expected Poisson contraction during simple tension thus maintaining zero pressure on the free surfaces. Deactivating the pressure controller produced a constrained tension test, while photographic dimensional changes in all three directions produced a bulk strain test.

Stresses were measured by summing all the forces passing through the deformed but planar faces of the computational box, while keeping track of their vector components. The outward directed component, divided by the appropriate area, was taken as the normal stress on that face, while the shear stresses were computed from the two in-plane force components. Symmetry of the periodic boundaries allow for only 9 unique stresses. The shear stresses on adjacent faces of the cube were not found to be equal at any given instant because at finite temperatures, the elemental cube of 256 atoms does indeed rotate. The time-average shear stresses were, of course, found to be zero when no shear deformations were applied.

Shear deformations were implemented differently. Rather than actually moving the atoms to the locations corresponding to a sheared configuration, the forces between atoms that would be caused by shearing the system, including the periodic boundary cells, were computed and integrated to determine the subsequent forces, positions and stresses. In this way, the superstructure of the program for implementing the periodic boundary conditions and for computing the stress tensor could be used unchanged during a shear test. No measurable normal stresses developed during shear testing at strains up to 1%. Normal stresses did develop at shear strains approaching 10% as a result of the volume decreases associated with large magnitude pure shear strains.

The strain tensor was calculated from the true strains based on the dimensional and shape changes of the computational box relative to the initial dimensions at the beginning of a given test. In this way, the constant temperature and constant pressure conditions enforced during the first 100 iterations established the equilibrium dimensions of the system. This decision to base strains on the

initial reference state followed from the experimental concept of basing moduli on the unstressed dimensions at the temperature and pressure of interest.

Tests were conducted in such a way that the total strain applied to the specimen was 1%. This strain was always applied during 5000 iterations of testing. Testing was continued for an additional 100 iterations before moving to the data acquisition portion of the program so that artifacts of signal processing, such as the Gibbs phenomenon,¹⁹ could be excluded.

E. Data acquisition and digital filtering

To simplify data acquisition and output, all variables calculated for the system were stored at every iteration. Variables included the computational box sizes and shape, the stress tensor, the kinetic and potential energies, and the bulk stresses and strains. Thus, once the test was complete, the user could selectively examine any variable as a function of any other variable. An additional flexibility built into the program was the ability to apply different filtering schemes such as the causal and fast Fourier methods used in this paper. This is of particular value during manual operation and debugging. All data reported in this work were subjected to fast Fourier transform low-pass filtering using a 100-point window.^{17,19} For each type of test, several runs were made in manual mode with examination of trends in the data, constancy of temperature, constancy of lateral pressure, effect of initial conditions, etc. Once the code was complete, all runs used to produce data for this paper were completed using batch mode script files to input commands to the user friendly interactive interface. For every data set written to disk, various statistical tests were run, including linear regression to determine slopes and intercepts. Statistical measures were positioned as comments at the beginning of each 5000-point data file for easy cut and paste into the graphics routine used to plot the results. Solid bold lines in the graphs are composed of closely spaced individual data points, regression results are shown as dashed lines.

F. Execution speed

The constant-rate deformation tests described in this work (256 atoms, 3.0σ cutoff radius, 6100 iterations) were completed in slightly less than 1 h on a 15 MIP (millions of instructions per second) workstation. Thirty two Mbytes of memory allowed systems as large as 1000 atoms to be run. Execution time increases linearly with the number of atoms because of the nearest-neighbor look-up list methodology. This algorithm is fast enough to enable routine computation of elastic properties on workstations such as those that are available in the scientific and engineering communities.

III. RESULTS ON SINGLE-CRYSTAL ELASTIC CONSTANTS

A. Organization of results

In molecular-dynamics simulations, there is never a shortage of results. Since every variable is available for

scrutiny, the difficulty lies in compacting the results into meaningful figures. Large numbers of runs were made, each of which produced the six-component stress tensor, the temperature, and the potential energy as a function of the applied deformation variable. Each run could be conducted at constant temperature and/or constant pressure (aside from the axis under deformation), producing four sets of results. To represent the effect of test temperature, and in particular the thermal noise as related to testing constraints, results obtained at the highest temperature, the lowest temperature and an intermediate temperature for each case are shown. Results at temperatures in between are well represented by these behaviors. For each temperature, a single figure, composed of eight graphs is shown to represent the characteristic behaviors observed. Stress axes are all on a scale of $0-1\epsilon/\sigma^3$ and the strains applied to the sample during every test ranged from 0 to 1%, independent of the type of strain. The data lines are each composed of 5000 closely spaced opened diamond shaped points that form a bold line, making the data easy to see. Every data set has a dotted line through it which was fit by linear regression of the ordinate variable against the abscissa variable. The regressed slope of each line is included in each figure. The initial slope, based on the first 0.002 strain, is indicated by a superscript zero. The results from other calculational runs are assembled into a summary figure showing all the elastic property variations with temperature for isothermal tests. Adiabatic results for bulk straining are also included.

All tests were conducted with the [100] directions of the fcc Lennard-Jones system parallel to the principal testing directions. This is illustrated in Fig. 1, which shows the computational box in relation to the unit cell of the structure. The initial r_0 was set at 1.09240σ , less than $2^{1/6}=1.12246\sigma$ corresponding to the equilibrium spacing of two atoms. The compressional effect of second-, third-, and higher-nearest neighbors required this smaller initial atomic spacing in order to produce zero pressure at zero temperature. The unit cell, containing four atoms per cell, had an $a_0=1.54488\sigma$. The computational box was composed of four unit cells in each direction with net initial dimensions of $4a_0=6.17955\sigma$ on each side at 0 K and zero pressure. The computational box contained $4^3=64$ unit cells for a total of 256 atoms. Temperature and pressure control during pretesting equilibration at finite temperatures produced thermal expansions of the box. The average dimensions of the box over 500 iterations just prior to the beginning of a test were used as the initial reference size upon which strains were based.

Tensile tests were pulled in the X or 1 direction, while shear tests were conducted symmetrically on the YZ or 23 planes. The positive stress-tensor components shown in Fig. 1 establish the directions of the stresses and strains to be discussed below.

B. Tensile testing results

The results of uniaxial tension tests at constant temperature are shown in parts (a), (b), and (c) of Figs. 2, 3, and

4 for temperatures corresponding to kinetic energies per atoms of 0.005ϵ , 0.2ϵ , and 0.5ϵ , respectively. Because thermal noise increases monotonically with temperature, it is desirable to first examine the results obtained at $T=0.005\epsilon$. It is seen from Fig. 2(b) that $d\sigma_{22}/d\epsilon_{11}$ is operationally zero with a value of $0.002\epsilon/\sigma^3$. This indicates that the stresses $\sigma_{22}=\sigma_{33}$ were maintained at zero as a result of the operation of the pressure controller, implying that the slope of σ_{11} versus ϵ_{11} , as shown in Fig. 2(a), represents $1/S_{11}=E_{100}$, the Young's modulus in the [100] direction. Note that this curve appears to be exactly linear with a slope of $61.09\epsilon/\sigma^3$ as determined by the regression analysis. Figure 2(c) shows ϵ_{22} as a decreasing function of the axial strain, ϵ_{11} . The two lateral strains, ϵ_{22} and ϵ_{33} , are identical as a result of the scaling methods used to keep the lateral stress constant. It should be noted that Fig. 2(c) has an average slope over the 1% range of ϵ_{11} strain, which corresponds to a Poisson ratio of $\nu_{100}=0.347$. The compliance S_{12} can be obtained from a combination of E_{100} and ν_{100} because $S_{12}=-\nu_{100}/E_{100}$.

Regression over strains from 0 to 0.002 results in an initial value of the Poisson ratio of $\nu_{100}^0=0.361$. This approximates the limiting value at small strain. Because this limit cannot be obtained at present for the noisier finite temperature data, values without the zero superscript which represent the regression results over the 0 to 1% strain range are reported instead in order to examine the temperature dependencies of the elastic properties.

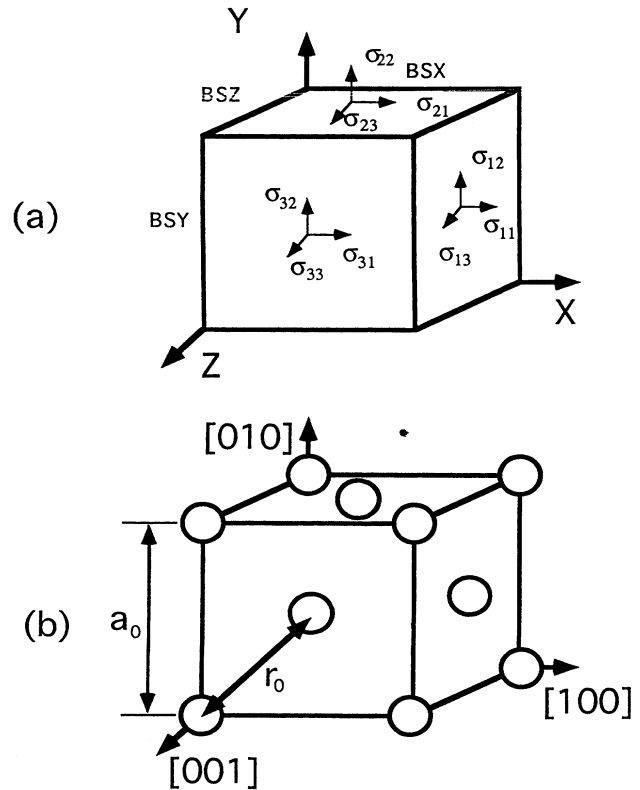


FIG. 1. (a) Computational box showing stress-tensor orientation. (b) fcc unit cell used to generate initial atom locations by repetitive translations.

Parts (a), (b), and (c) of Figs. 3 and 4 show the results of increasing temperature on the measured stress versus strain and strain versus strain responses. Notice in Fig. 3 that a long-wavelength oscillation appears to be developing, which is reflected in both the σ_{11} versus ε_{11} and ε_{22} versus ε_{11} plots, in a complementary sense, reflecting the desire of the system to conserve its volume. As expected, higher-frequency oscillations are seen in Fig. 3(b) indicating that the pressure controller is responding to the thermal variations. At the highest temperature, 0.5ε , the long-wavelength oscillations are also present but are strongly overshadowed by the increased amplitude of the higher-frequency thermal noise. Because every sample was equilibrated in exactly the same way and thus had identical initial conditions prior to testing, it is interesting to note the presence of correlations between the noise responses in tension and those in shear. An example is seen in the somewhat symmetric behaviors about the 0.0025 strain point [compare Figs. 4(a) and 4(d)] that occur at exactly the same number of iterations from the

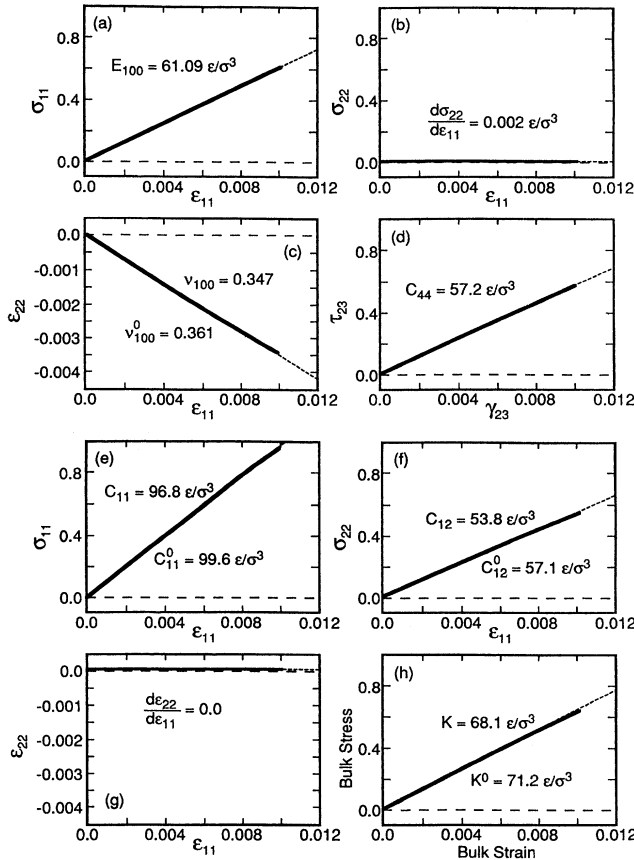


FIG. 2. Computed mechanical responses at 0.005ε . (a) Uniaxial stress-strain curve. (b) Verification of the free surface condition. (c) Lateral contraction due to the Poisson effect. (d) Shear stress shear strain response. (e) Biaxially constrained tension test with (f) lateral stress needed to produce no change in (g), the lateral strain versus the axial strain. (h) Hydrostatic tension test. Insets denote slopes regressed over 1% strain. When nonlinearity is noted, the initial slopes over the first 0.2% strain are given as indicated by a superscript zero.

onset of testing. Thus, it is quite likely that the noise remaining in these curves originates from the initial conditions as a wave structure or phonon distribution which then propagates through the system by virtue of the periodic boundary conditions. The details of the noise structure are responsible to the initial conditions as reflected by the number of iterations used to equilibrate the system. Equilibration for 2000, 3000, 4000, etc. iterations produces similar behavior in terms of moduli, but with different noise structures. Further attention to the noise spectra will be given in the discussion.

It should be noted that the compliances can be obtained from these two directionally defined parameters in that $S_{11} = 1/E_{100}$ and $S_{12} = -\nu_{100}/E_{100}$.

C. Shear testing

An independent set of deformations was used to calculate the shear stress τ_{23} , representing the average value of the τ_{yz} and τ_{zy} entries of the stress tensor as a function of the applied shear strain γ_{23} . The shearing was performed symmetrically so that $\varepsilon_{23} = \varepsilon_{32} = \gamma_{23}/2$. Again, noteworthy is the extreme linearity of τ_{23} as a function of γ_{23} , as displayed in Fig. 2(d), with a slope of

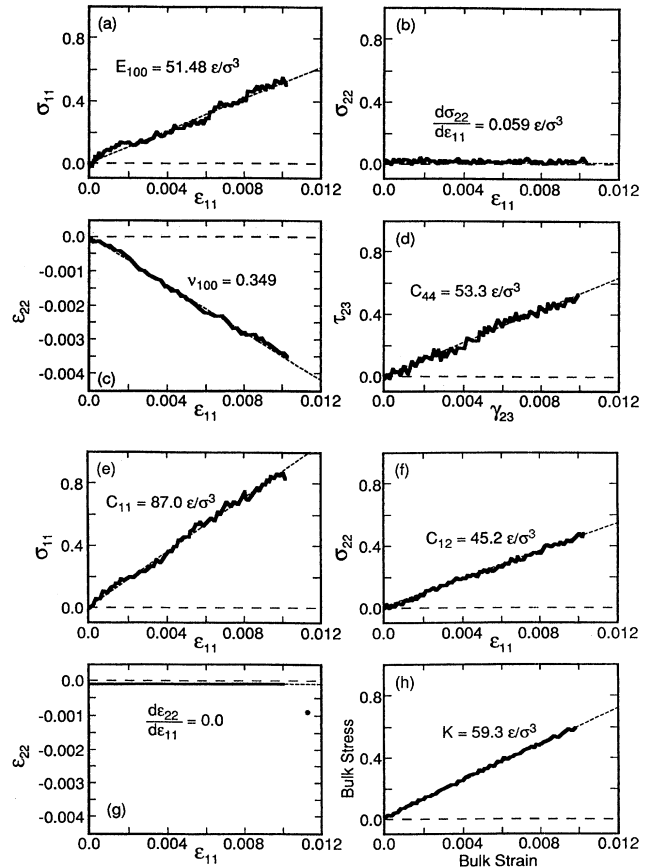


FIG. 3. Computed mechanical responses at 0.2ε . Note the increase in thermal noise and decrease in stiffness relative to the lower temperature data in Fig. 2. See caption to Fig. 2 for additional description for each part of this figure.

$C_{44} = 1/S_{44} = G_{100} = 57.21\epsilon/\sigma^3$. Thus these same values represent the initial slope values, C_{44}^0 , S_{44}^0 , and G_{100}^0 . With increasing temperature, both long- and short-wavelength oscillations appear in the shear stress versus shear strain curves, indicative of both thermal noise and shear wave activity within the sample.

D. Constrained tension test

Parts (e), (f), and (g) of Figs. 2, 3, and 4 show results of constrained tension tests for each of the three temperatures. Part (g) illustrates the constraint during the test, showing that no change in the lateral strains $\epsilon_{22} = \epsilon_{33}$ occurred. Slight shifts such as that shown in Fig. 3(g) occur as a result of variations in strain during the pretest of the equilibration of pressure. At $T = 0.005\epsilon$, the effect of the constraint is apparent as a concave down behavior of both σ_{11} and $\sigma_{22} = \sigma_{33}$ as a function of ϵ_{11} . The slopes of these curves over the range of 0 to 1% are the stiffnesses $C_{11} = 96.81\epsilon/\sigma^3$ and $C_{12} = 53.78\epsilon/\sigma^3$, respectively. When only the initial portions are considered, these values increase to $C_{11}^0 = 99.56\epsilon/\sigma^3$ and $C_{12}^0 = 57.07\epsilon/\sigma^3$. While this same tendency to be concave down should be

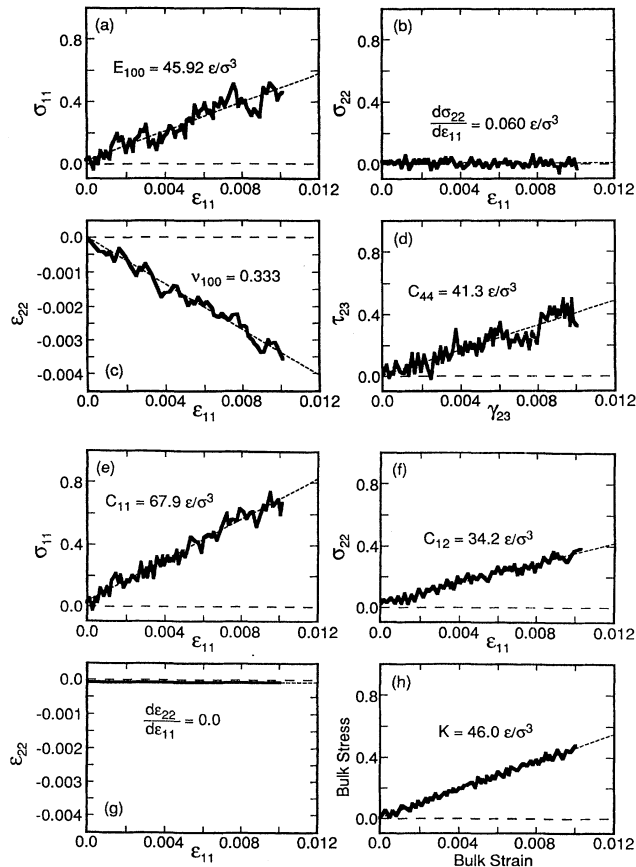


FIG. 4. Computed mechanical responses at 0.5ϵ . Note the continued decrease in stiffness and increase in thermal noise at this, the highest temperature evaluated. Slopes are obtained by linear regression of the 5000 data points making up each curve. See caption to Fig. 2 for additional details.

present at higher temperatures, it cannot be discerned easily due to the noise present in the data. Again it is observed that the variations in the behavior with increasing temperature have both a long term oscillation as well as a shorter-wavelength component that scales with the temperature.

E. Bulk stress tests

Part (h) in Figs. 2, 3, and 4 show the bulk stress, $(\sigma_{11} + \sigma_{12} + \sigma_{33})/3$, as a function of the bulk strain, $\Delta V/V = \epsilon_{11} + \epsilon_{22} + \epsilon_{33}$, when the sample is responding to hydrostatic tension. In these runs, the three strains were held equal by incrementally incrementing the principal dimensions of the computational box, while the stress values required for equilibrium were calculated. Because of the symmetry, no appreciable shear stresses were developed. The shape of this curve is again concave down as a result of the constraints causing the distances between atoms to increase sufficiently to exhibit the non-linearity of the potential. The slopes of this curve are $K = 68.07\epsilon/\sigma^3$ and $K^0 = 71.22\epsilon/\sigma^3$. While thermal noise develops in this instance as well, it is clear that the magnitude of the thermal noise is substantially smaller for the bulk stress/bulk strain behavior. This is a result of the fact that no error is present in the bulk strain as the independent variable and that all three stresses are averaged producing a statistically larger number of atoms in the average.

F. Temperature dependence of elastic properties

Figure 5 presents the composite temperature dependences of the isothermal elastic constants, C_{11} , C_{12} ,

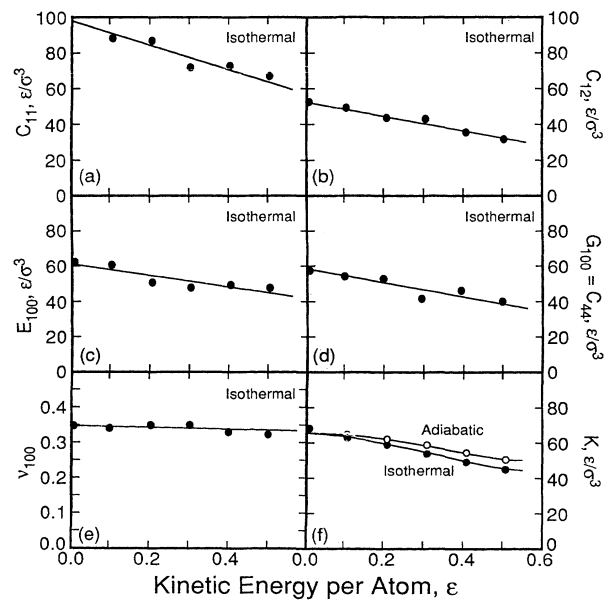


FIG. 5. Temperature dependences of the single-crystal elastic properties of a fcc Lennard-Jones solid computed under isothermal conditions by regression over first 1% of axial strain. Adiabatic results for bulk modulus are also provided.

$C_{44} = G_{100}$, E_{100} , ν_{100} , and K over the range of testing temperatures 0.005–0.5 ϵ . These elastic constants were determined by regression analysis of the data over the first 1% of the appropriate stress-strain curves. Had it been possible to calculate the initial slopes, it is likely that all the stiffnesses would be larger by approximately the ratios characteristic of the lowest temperature case. Variation in the data are a result of noise in the data which produce occasional fluctuations in the shape of the stress-strain behavior. As a result, the elastic constant data have been fit with a single dashed line passing through the centroids of the first three and last three data points to serve as a guide to the eye in assessing the temperature dependence for all but the bulk stress versus bulk strain behavior. For the latter case, the thermal noise was sufficiently small so as to allow the shape of the curve to be visible. Accordingly, a smooth curve was fit with a draftsman's spline, satisfying the condition of zero slope at zero temperature by ignoring the lowest data point. This is justifiable because at the lowest temperature, the atoms do not have sufficient thermal speeds to maintain equilibrium behavior in comparison with the deformation speeds of the present test. Therefore, the zero Kelvin results would have overestimated the elastic stiffnesses. The general features of the temperature dependence of the bulk modulus are in agreement with data for single-crystal zinc.²⁰

Because these data were well behaved, it was also possible to determine the adiabatic bulk moduli by performing the same series of calculations with the temperature controller disabled at the start of the test. Examination of the temperature as a function of strain showed that the temperature of the adiabatic sample decreased a total of 4% during the 1% volumetric strain experiment causing the temperature to change from 0.50+0.48 ϵ during the test at the highest temperature. Results at lower temperatures were proportional as can be seen by comparing the isothermal and adiabatic results in Fig. 5.

G. Polycrystalline aggregate properties

A polycrystalline aggregate composed of randomly oriented single-crystal grains, each exhibiting the single crystalline elastic properties, will behave as a macroscopically isotropic material. The elastic properties of the single crystals may be averaged under the assumptions of constant strain or constant stress. Averages of the stiffnesses, assuming constant strain, were performed by Voigt,²¹ while averages of the compliances, assuming constant stress, were performed by Reuss.²² These Voigt and Reuss averages of the elastic stiffnesses (C_{ij}) and compliances (S_{ij}) were shown to be bounds for aggregate behavior by Hill.²³ Since then, Hashin and Shtrikman²⁴ have developed improved bounds on the elastic compliances and stiffnesses of aggregates made from cubic materials. In many cases, the upper and lower bounds are sufficiently close as to prescribe the value. This work was well documented by Simmons and Wang.¹² For reasons of self containment of this paper, their tabulations are presently reproduced.

The Voigt and Reuss averages are given by

$$\begin{array}{ll} \text{Voigt} & \text{Reuss} \\ K_V = (A + 2B)/3, & K_R = 1/(3a + 6b), \\ G_V = (A - B + 3C)/5, & G_R = 5/(4a - 4b + 3c), \end{array}$$

where (2)

$$\begin{array}{ll} 3A = C_{11} + C_{22} + C_{33}, & 3a = S_{11} + S_{22} + S_{22}, \\ 3B = C_{23} + C_{31} + C_{12}, & 3b = S_{23} + S_{31} + S_{12}, \\ 3C = C_{44} + C_{55} + C_{66}, & 3c = S_{44} + S_{55} + S_{66}, \end{array}$$

Hashin and Shtrikman²⁴ showed that the Voigt and Reuss bounds could be improved, and they developed expressions for the corresponding bounds of aggregates of cubic crystals. For a single-phase aggregates of a cubic material, the bulk modulus K is given unambiguously by

$$K = (C_{11} + 2C_{12})/3, \quad (3)$$

and the shear modulus is bounded by

$$G_1^* = G_1 + 3\{[5/(G_2 - G_1)] - 4\beta_1\}^{-1}, \quad (4)$$

and

$$G_2^* = G_2 + 2\{[5/(G_1 - G_2)] - 6\beta_2\}^{-1}, \quad (5)$$

where

$$\beta_1 = -3(K + 2G_1)/[5G_1(3K + 4G_1)], \quad (6)$$

$$\beta_2 = -3(K + 2G_2)/[5G_2(3K + 4G_2)],$$

$$G_1 = (C_{11} - C_{12})/2,$$

$$G_2 = C_{44},$$

and the C_{ij} are the usual single-crystal elastic stiffnesses.

Because relations between E , K , G , and ν are well known for isotropic materials,²⁵ the bounds on G produce the following bounds on E and ν :

$$\begin{array}{l} \nu_H = (3K - 2G_H)/(6K + 2G_H), \\ \nu_S = (3K - 2G_S)/(6K + 2G_S), \\ E_H = 3K(1 - 2\nu_H), \quad E_S = 3K(1 - 2\nu_S). \end{array} \quad (7)$$

Using these expressions, the elastic stiffness results C_{11} , C_{12} , and C_{44} are combined at each temperature to produce the temperature dependence of the Hashin and Shtrikman bounds. As shown in Fig. 6, the upper and lower bounds for a polycrystalline aggregate of fcc Lennard-Jones material are sufficiently close that they effectively determine the values of the elastic properties. These isotropic parameters are substantially different from the E_{100} , G_{100} , and ν_{100} that were used to represent the compliance data for the single-crystalline form in the [100] direction. These polycrystalline isotropic results represent the elastic property data for a Lennard-Jones material in a way that can be easily compared with the elastic properties of real materials that are often modeled by the Lennard-Jones potential.

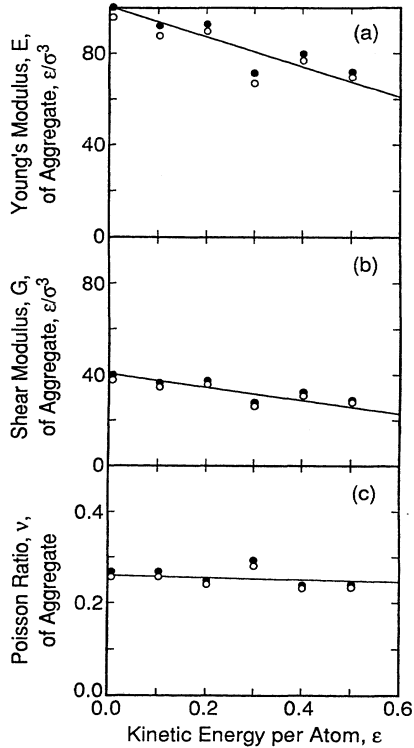


FIG. 6. Hashin and Shtrikman bounds for the elastic properties of polycrystalline Lennard-Jones material based on fcc structure and computed single-crystalline behavior. Note that the Poisson ratio is 0.25 for this central force and isotropic material.

IV. DISCUSSION

A. Stresses and Cauchy relationships

Early in the development of the mathematical theory of elasticity, people such as Navier, Cauchy, and Poisson concerned themselves with how a material composed of hypothetical molecules might respond to external loads. The idea that “the elastic properties of solids can be explained in terms of some attractive and repulsive forces between their ultimate particles”²⁶ has existed from the time of Newton. Poisson began the serious exploitation of this concept by attempting to model a plate with a single layer of molecules in 1812.²⁶ Cauchy introduced the concepts of replacing action at a distance with contact action in the definition of the Cauchy stresses, based primarily on his earlier experience in hydraulics. This was a very fundamental and philosophical change²⁷ in how one thinks about the transmission of stresses in solids composed of atoms and molecules and is likely to have a profound effect on our ability to understand the behavior of materials at small size scales.

In what amounts to an analytical estimate of moduli arising from the interaction between discrete particles, Poisson²⁹ cautioned that the dimensions of the parallelepiped by which the stress, later to be known as the Cauchy stress, was defined must be large compared to the radius of activity (the cutoff radius) of the molecules. This

warning highlighted the limitations of the assumption made by Cauchy that action at a distance can be replaced by contact action in order to facilitate the definition of stress. At small size scales, the definition of the Cauchy stress breaks down. In the present case, the periodic boundary conditions make our samples effectively infinite in dimension. However, because of the treatment of spatial variations in stress, the concept of Cauchy stresses cannot be used at dimensions comparable to the cutoff radius. For these calculations a large area is needed to average the stress in order to produce a value that is noise free unless one provides for equivalently long temporal averaging.

Cauchy’s treatment of the anisotropic elasticity of materials having a center of symmetry and interacting by central forces produced a set of six relationships²⁸

$$\begin{aligned} C_{23} &= C_{44}; & C_{56} &= C_{14} & C_{64} &= C_{25}, \\ C_{31} &= C_{55}; & C_{12} &= C_{66}; & C_{45} &= C_{36}, \end{aligned} \quad (8)$$

which he assumed to be valid for all materials. This assumption led to the conclusion that only 15 elastic constants were needed to represent the elastic properties of crystals of arbitrarily complex spatial arrangements, rather than the 21 now commonly associated with triclinic materials. Because many of the current molecular modeling concepts were not available then, it seemed plausible to hypothesize that central forces could produce any arbitrary arrangement. Now it is understood that central forces also lead to closest packing, thereby restricting the number of possible structures. To obtain triclinic structures or other less fully dense structures may require antibonding density-functional contributions to the potentials, which will produce noncentral forces. Alternatively, bonding density functionals can lead to violation of the Cauchy relationships thereby enabling better representation of the single-crystal elastic behaviors of real cubic materials by raising the Young’s modulus relative to the shear modulus. Exploring the Cauchy relationships is a useful exercise aimed at understanding the origin of shear resistance in crystalline materials.

The Cauchy relations can be interpreted as physically representing the molecular level cross bracing that results from central forces. Consider a small two-dimensional crystal where atoms 1, 2, 3, and 4 are at the corners of a square array as shown in Fig. 7. Loads P_x and Q_x are applied to the X faces, while loads P_y and Q_y are applied to the Y faces. The crystal is in equilibrium in that the attractive forces across the diagonals are opposed by repulsive forces along the edges. If the interatomic force law is arbitrary, it is likely that the two types of spacing, a_0 , and $\sqrt{2}a_0$, will have different stiffnesses. Denote them by k and K , respectively, as shown in Fig. 7.

Now consider an axial extension in the X direction by an ϵ_{xx} with the constraint that ϵ_{yy} remains zero, as would be necessary to calculate C_{11} and C_{12} . This is shown in the central portion of Fig. 7. The total forces Q_x and Q_y are zero. The length changes of the 12 and 34 bonds are $a_0\epsilon_{xx}$, while the length changes of the 14 and 32 bonds are $\sqrt{2a_0^2 + a_0^2(1 + \epsilon_{xx})^2} - \sqrt{2}a_0$, which, for small strains, are approximately $\sqrt{2}a_0\epsilon_{xx}/2$. By combining

these changes in length with the stiffness, it is found that

$$\begin{aligned} F_{12} &= ka_0 \epsilon_{xx} , \\ F_{13} &= 0 , \\ F_{14} &= K\sqrt{2}a_0 \epsilon_{xx} / 2 , \end{aligned} \quad (9)$$

where F_{ij} designates the force between atoms i and j . The total normal forces needed to balance these internal forces are

$$\begin{aligned} P_x &= 2F_{12} + 2F_{14} \cos 45^\circ = (2ka_0 + Ka_0) \epsilon_{xx} , \\ P_y &= 2F_{13} + 2F_{14} \sin 45^\circ = Ka_0 \epsilon_{xx} . \end{aligned} \quad (10)$$

Now consider the shear as shown in the lower portion of Fig. 7. For small strains, only the diagonal bonds change length. These bonds change length by $\sqrt{2}a_0\gamma/2$

with bond 23 increasing and bond 14 decreasing. Combining these expressions with the stiffnesses one finds that the forces are

$$\begin{aligned} F_{12} &= F_{13} = 0 , \\ -F_{14} &= F_{23} = K\sqrt{2}a_0\gamma/2 , \end{aligned} \quad (11)$$

where a positive force represents attraction. These forces are balanced by the components of Q_x and Q_y so that

$$Q_x = Q_y = F_{23} \cos 45^\circ - F_{14} \cos 45^\circ$$

or

$$Q_x = Q_y = Ka_0\gamma . \quad (12)$$

Letting $\sigma_x = P_x/a_0$, $\sigma_{yy} = P_y/a_0$, and $\tau_{xy} = (Q_x + Q_y)/2a_0$, and assuming unit thickness to express the problem in terms of stress, yields

$$\begin{aligned} \sigma_{xx} &= (2k + K)\epsilon_{xx} + K\epsilon_{yy} = C_{11}\epsilon_{xx} + C_{12}\epsilon_{yy} , \\ \sigma_{yy} &= K\epsilon_{xx} + (2k + K)\epsilon_{yy} = C_{12}\epsilon_{xx} + C_{11}\epsilon_{yy} , \\ \tau_{xy} &= K\gamma_{xy} = C_{44}\gamma_{xy} . \end{aligned} \quad (13)$$

Equating coefficients shows that $C_{11} = 2k + K$, and $C_{12} = C_{44} = K$. The relation between C_{12} and C_{44} is the Cauchy relation for this simple system. In the full three-dimensional cubic case, crystal symmetries reduce the Cauchy relations of Eq. (8) to this same independent expression, namely $C_{12} = C_{44}$.²⁸ Consequently, it can be seen for these cases, that the Cauchy relation is a result of cross bracing of the structure by the central forces. In addition, it can be seen that it is this cross bracing by central forces that produces the shear resistance rather than the shear resistance arising from the bending of bonds. These Cauchy relations can be generalized to other systems as well and show that the three-dimensional character of the structures are sufficient to produce shear resistance through central forces in much the same way that a three-dimensional truss supports shear loads. The addition of cohesive interactions that responds to local density allows for increases or decreases in bulk modulus without a shear resistance change and this effect produces a violation of the Cauchy relations. It also allows for the possibility of nonclose-packed crystal structures by providing a driving force for lower-density structures. This will be more fully discussed later in this paper.

Examination of the temperature dependences of C_{12} and C_{44} in Fig. 5 in combination with the shape of the stress-strain responses in Fig. 2, show that the Cauchy relations are fully satisfied for the Lennard-Jones solid. The shear response is essentially linear, while the stress-strain relationship corresponding to C_{12} is concave down. Noting that the initial slope C_{12}^0 is about $3\epsilon/\sigma^3$ larger than the slope obtained by fitting the data over the first 1% strain and applying this as a correction to the entire temperature dependence of C_{12} shows that the Cauchy relation $C_{12} = C_{44}$ is true over the entire temperature range examined. Given this, it is curious to note that the variations in the temperature dependences of these stiffnesses relative to the dashed trend lines shown in Fig.

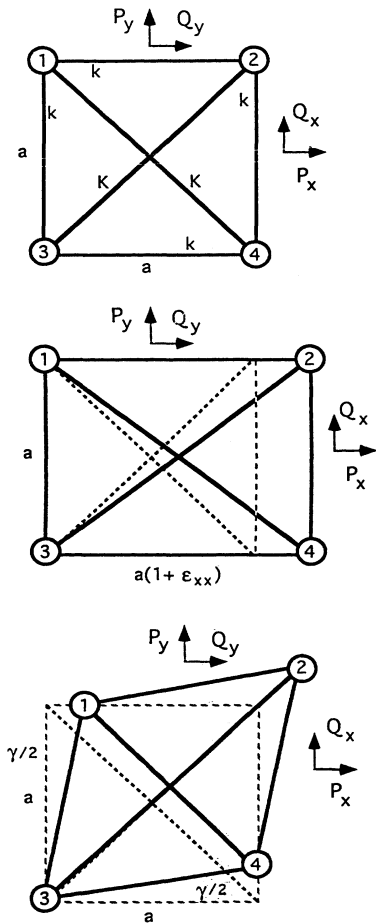


FIG. 7. Two-dimensional square lattice used to illustrate the (a) original dimensions and stiffness coefficients of the individual bonds, (b) the changes in bond length due to laterally constrained extension, and (c), the changes in bond lengths due to shear deformation. These figures are used to document that molecular level cross bracing by central forces is responsible for the links between shear stiffness and the specific degree of Poisson contraction known as the Cauchy relations, $C_{12} = C_{44}$.

5 are in the opposite sense. Therefore, averaging these parameters to obtain an improved estimate of their temperature dependence would be beneficial.

Both Poisson²⁹ and Navier²⁶ implicitly assumed isotropic behavior in their calculations of the differential equations of equilibrium. They did this by assuming that the spatial orientation of any given molecular interaction was equally probable in all directions. As discussed previously, this is functionally equivalent to producing the results associated with a polycrystal formed from a material composed of molecules interacting by central forces. This is the case for the results presented in Fig. 6. For a material that obeys the Cauchy relations and is also spatially isotropic, the relations between the elastic constant become extremely restricted. Indeed, only a single elastic constant represents their behavior as is shown below.

B. Cauchy solid

Defining a cubic material that obeys the Cauchy relations as a Cauchy solid, it is clear that only two of the three elastic constants normally needed for a cubic material are independent, namely C_{11} and $C_{12} = C_{44}$. By writing the compliances in terms of stiffnesses and relating them to E_{100} , ν_{100} , and G_{100} , it is possible to show that, for a Cauchy solid,

$$G_{100} = [2\nu/(1-2\nu_{100})]E_{100}/[2(1+\nu_{100})]. \quad (14)$$

Within computational uncertainty, the data in Fig. 5 is consistent with this expression. Thus only two elastic constants are needed to express the elastic properties of a cubic Lennard-Jones solid because of the fact that the Cauchy expressions are satisfied. If one now imposes the constraint of isotropy in the same way, one obtains the familiar expression for shear modulus in terms of the Young's modulus and Poisson ratio,

$$G = E/[2(1+\nu)]. \quad (15)$$

Here, the requirement of spatial isotropy has reduced the number of independent elastic constants to two by applying the particular symmetry rules associated with isotropy.³⁰ When a material satisfies both of these requirements, comparison of the two expressions for G shows that $\nu = \frac{1}{4}$ and $G = 2E/5$. An examination of Fig. 6, depicting the polycrystalline bounds on the elastic behavior, shows that such calculations bear out this result. It is clear that an E of $100\epsilon/\sigma^3$ corresponds to a G of $40\epsilon/\sigma^3$, and that ν is approximately 0.25 at all temperatures. This information could be used to improve one's ability to reduce the noise in the present calculations. In particular, because only one constant is needed, choosing that constant to be the bulk modulus, which is uniquely the same for cubic single crystals and polycrystals alike, is very attractive. Combining the choice of K with the fact the ν must be $\frac{1}{4}$ allows us to express any other elastic constant in terms of K and ν .²⁵ Thus, assuming isotropy, we have for $\nu = \frac{1}{4}$

Isotropic solid	Isotropic Cauchy solid
$E = 3(1-2\nu)K$	$= 3K/2$
$\mu = G = 3(1-2\nu)K/[2(1+\nu)]$	$= 3K/5$
$\lambda = 3K\nu/(1+\nu)$	$= 3K/5$

(16)

where λ and μ are the Lamé constants representing isotropic elastic behavior. This particular case of $\lambda = \mu$ is known as the "Poisson relation"³¹ in reference to Poisson's notion that $\nu = \frac{1}{4}$ for all materials, a notion that persisted for quite some time.³² The assumptions leading to this result are discussed more fully elsewhere.³³

The relationships developed here clearly show that only a single elastic constant is needed for isotropic bodies composed of central-force molecules. Navier and Poisson were correct for the isotropic behaviors they were modeling. Cauchy was also correct for the anisotropic central-force systems that he postulated. They were amazingly correct given that they did not have proof that molecules existed. For a cubic single crystal composed of central-force molecules, the Cauchy relations are obeyed and only two elastic constants are needed to represent the elastic properties.

C. Limiting behavior at zero temperature

In this paper, it appears that the bulk modulus K has both isotropic and adiabatic behaviors that smoothly approach absolute zero temperature with zero slope as required by thermodynamics. However, in examining the lowest temperature calculations at 0.005ϵ in Fig. 5, one notes that the bulk modulus has been overestimated because of the inability of the system to maintain equilibrium at such low temperatures. Individual atoms are not moving fast enough compared with the rates of change of the shape of the computational box. Computations at lower temperatures, such as $10^{-6}\epsilon$, produce noise free stress-strain curves with stiffnesses that continue to increase with decreasing temperature, supporting this hypothesis. Further work is planned to examine the low-temperature behavior, particularly those involving thermal expansions and specific heats.

D. Distinguishing between noise and sound

Periodic boundary conditions are generally required to model the behavior of bulk solids. This makes it necessary to address the consequences these conditions impose in terms of lattice vibrations. In particular it is desirable to distinguish between thermal noise and the momentary passage of a sound wave. In a system with periodic boundaries, a plane sound wave which does not show dispersion will traverse the region of interest repeatedly in a coherent fashion. If there is dispersion, the various components will revisit but not coherently. As it happens, waves of different types, such as shear and longitudinal waves, travel at different speeds and numerous waves can coexist in the same space. One could take the approach that all the atomic displacements are the result of a specific sampling of sound waves. However, it is clear that periodic interactions of these traveling waves can modify the stress-strain results and in effect limit the

sampling of momentum space explored by a given molecular-dynamics model. Moreover, models are sensitive to initial conditions that trap specific modes of longitudinal and shear vibrations within the periodic boundaries. The solution to this dilemma appears to be to allow the system to communicate its momentum distribution with an infinite reservoir that maintains statistical validity without actually modeling the infinite system. The justification for this approach comes from the fact that small volumes in a solid interact by radiation, a fundamentally bulk process.³⁴ This will allow a small system to continuously explore different regions of momentum space so that temporal averaging will produce statistically valid results, rather than results confounded by periodic waves. To do this, however, requires that the sources of the apparent sound/noise interactions be determined and the periodic character removed. One can begin this process by examining the wave speeds.

E. Wave speeds

The speeds of waves, both longitudinal and shear, are related to the elastic constants of isotropic materials by

$$C_l = \sqrt{(\lambda + 2\mu)/\rho}$$

and (17)

$$C_s = \sqrt{\mu/\rho}.$$

For single-crystalline materials, the wave speeds in specific directions can be calculated from the detailed elastic constants of the crystal system. However, for the present problem we do not know in which direction the waves are traveling. It will be assumed that the isotropic values will suffice to determine the phonon velocities, from which the transit times of waves can be estimated. For our Lennard-Jones solid we note that $\lambda = \mu$ so that $C_l = \sqrt{3}C_s$.

To calculate the mass density, it is known that the 256 atoms, each of mass m , occupy the computational box of initial dimensions 6.17955σ . Thus $\rho = 256m / (6.17955\sigma)^3 = 1.08485m/\sigma^3$.

Noting from Fig. 6 that the isotropic shear modulus varies from $40\epsilon/\sigma^3$ at zero temperature to $25\epsilon/\sigma^3$ at a temperature of 0.6ϵ , it is clear that changes in the shear wave speed with temperature cause it to vary over a range from $6.072\sigma/(\sigma\sqrt{m/\epsilon})$ to $4.800\sigma/(\sigma\sqrt{m/\epsilon})$. Selecting $5.5\sigma/(\sigma\sqrt{m/\epsilon})$ as a typical value, the time for such a shear wave to traverse the 6.17955σ computational box is

$$\begin{aligned} \Delta t &= 6.17955\sigma / 5.5\sigma / (\sigma\sqrt{m/\epsilon}) = 1.124\sigma\sqrt{m/\epsilon} \\ &= 113 \text{ iterations,} \end{aligned}$$

because each iteration is $0.01\sigma\sqrt{m/\epsilon}$. Because the compressional waves are $\sqrt{3}$ faster, they would require 65 iterations to cross the computational box. By examining the periodicity of the noise structures, one can attempt to make some correlations between periodic noise in the stress-strain response and the presence of traveling waves, either shear or compressional, in the sample. The noise present in the computational model is a result of

the initial assigned random velocity components that were not correlated with the deviation of the molecules from their mean positions on the lattice sites.

In examining Figs. 3 and 4 where the noise in the stress-strain data can be observed as oscillations in stress as a function of the 5000 iterations that occurred during each test. The number of peaks (37) implies that each wavelike oscillation takes $5000/37 = 135$ iterations. The data filters used involved smoothing over a 100-iteration-wide window so that variations faster than 100 iterations would be eliminated. In selecting this window width, sample data at 0.5ϵ was observed and the window modified until the worst case data still appeared to have a well defined and characteristic linear appearance. This window width was chosen because the remaining noise serves as proof that the results had not been oversmoothed thereby modifying the slopes obtained with this analysis technique.

It can be concluded therefore that the wavelength of the oscillation, while consistent with the motion of shear waves, are strongly influenced by the window width of the filter. The origin of the waves is a result of interference between the many waves and phonons present within the computational box. As shown in Fig. 4, there are clear correlations between the noise spectra, particularly the more slowly varying components, present in the axial and lateral directions. Considering that all tests at a given temperature started with exactly the same thermal history, including the details of the atomic velocities, the initial correlations between axial straining and shear testing are also significant. These observations strengthen the concept that traveling waves are playing a role in establishing the noise spectra in this data. Further work is needed to address the issue of allowing the phonon spectra to change dynamically thereby assuming a temporal distribution that does not reflect the periodicity of the boundary conditions.

It is also clear from an examination of the noise spectra in Figs. 3 and 4 that the addition of constraints decreases the apparent noise. This is possibly related to the fact that, as the number of constraints increases, the number of atoms being included in the averaging scheme also increases. Temporally correlated noise on adjacent faces resulting from Poisson contractions of traveling waves would tend to cancel one another in the bulk strain test where the noise levels were smallest. Increasing the number of atoms in the calculation to 864 did not produce such dramatic improvements as did the averaging over more sides during the bulk stress test. It is possible that the larger systems have longer times of flight and thus more noise was allowed through the 100-point-wide filtering window. Thus it appears that multiple tests of smaller samples may be a more efficient way to suppress noise in practical computations.

F. Comparison with real materials

The Lennard-Jones potential is often used to model various physical properties of argon. As a verification of the modeling reported here, the predicted elastic constants of argon are compared with experimental values.

In addition, the results are also compared with the predictions for a crystalline polymer (polyethylene).

The modeling parameters for argon are $\epsilon/k = 125$ K, $\sigma = 3.446$ Å, and $m = 39.9$ g/mol,³⁵ while those of polyethylene are $\epsilon/k = 225$ K, $\sigma = 4.19$ Å,¹¹ and $m = 28.0$ g/mol for the monomer unit. The polyethylene data is obtained from polarizability and molar diamagnetic susceptibilities, an approach which provides good estimates for the surface free energies of polymers whose monomer units contain less than five principal centers of attraction.¹¹ The magnitude of the moduli, in terms of ϵ/σ^3 , are 4.215×10^7 Pa for argon and 4.221×10^7 Pa for polyethylene. Rounding these off to two significant figures results in both having $\epsilon/\sigma^3 = 42.2$ MPa. Therefore the data calculated using the model for bulk argon compares essentially one to one with the following data for polycrystalline argon reported as limiting bounds in Ref. 12. Thus, at 4.2 K,

$$\begin{aligned} E &= 4.3 \times 10^3 \text{ MPa}, \quad G = 1.7 \times 10^3 \text{ MPa}, \\ K &= 2.7 \times 10^3 \text{ MPa}, \\ \nu &= 0.232 - 0.234, \quad \rho = 1.77 \times 10^3 \text{ kg/m}^3, \end{aligned}$$

at 76.8 K,

$$\begin{aligned} E &= 2.6 \times 10^3 \text{ MPa}, \quad G = 1.0 \times 10^3 \text{ MPa}, \\ K &= 1.8 \times 10^3 \text{ MPa}, \\ \nu &= 0.259 - 0.262, \quad \rho = 1.6451 \times 10^3 \text{ kg/m}^3. \end{aligned}$$

The polycrystalline results calculated with this model when translated to SI units for $\epsilon/\sigma^3 = 42.2$ MPa and $m = 39.9$ g/mol are at (0.6 K),

$$\begin{aligned} E &= 4.30 \times 10^3 \text{ MPa}, \quad G = 1.69 \times 10^3 \text{ MPa}, \\ K &= 2.78 \times 10^3 \text{ MPa}, \end{aligned}$$

(at 0.005 ϵ),

$$\begin{array}{ccc} (102\epsilon/\sigma^3) & (40.0\epsilon/\sigma^3) & (65.8\epsilon/\sigma^3) \\ \nu = 0.260 & \rho = 1.76 \times 10^3 \text{ kg/m}^3 & \end{array}$$

at (75 K),

$$\begin{aligned} E &= 2.47 \times 10^3 \text{ MPa}, \quad G = 1.00 \times 10^3 \text{ MPa}, \\ K &= 1.89 \times 10^3 \text{ MPa}, \end{aligned}$$

(at 0.6 ϵ),

$$\begin{array}{ccc} (58.5\epsilon/\sigma^3) & (23.7\epsilon/\sigma^3) & (44.9\epsilon/\sigma^3) \\ \nu = 0.246 & \rho = \text{not available} & \end{array}$$

Here the dimensionless values are shown in parenthesis. Comparison of these data with the computed bounds shown in the previous table indicate agreement for polycrystalline argon comparable with the round-off error in the reported bounds.¹² The calculated data used here are from the polycrystalline results trend lines in Fig. 6 extrapolated to 0.6 ϵ for comparison at 75 K.

Calculated single-crystal results do not match closely

with the reported experimental results of Gsanger, Egger, and Luscher,³⁶ despite the fact that these data are used to compute the bounds for argon. These experimentalists expressed surprise at the high value of C_{11} that they reported. The above calculations produce a value of $C_{11} = 4.09 \times 10^3$ MPa compared to the 5.29×10^3 MPa reported by Gsanger, Egger, and Luscher.³⁶ Conversely, the value $C_{12} = C_{44}$ presently calculated is 2.41×10^3 MPa, which is larger than 1.47×10^3 MPa, the mean of the C_{12} and C_{44} reported in Ref. 35 at 4.3 K. The bulk moduli are in excellent agreement with the value reported for the polycrystalline cases. Gsanger, Egger, and Luscher³⁶ measured only the sound velocities in [100] and [110] directions. They then combined their measurements with compressibility data that had been converted from isothermal to adiabatic and then corrected for temperature. In view of their procedure, the present agreement can be deemed reasonable.

Because the ϵ/σ^3 value for polyethylene is also 42.4 MPa, these same moduli values can be compared with data for polyethylene. The room temperature Young's modulus of HD polyethylene is $1.06 - 1.09 \times 10^3$ MPa.³⁷ Little data is available on the low-temperature elastic properties of polyethylene but it is likely that it will rise substantially with decreasing temperature, providing plausible agreement with the 2.47×10^3 MPa we calculated 75 K.

V. SUMMARY

The elastic properties of the fcc Lennard-Jones solid were determined by numerical experiments closely resembling those which would be used to make similar measurements on a physical system. The central-force closest-packed structure satisfied the Cauchy relations for cubic materials over the range of temperatures examined. The elastic constants measured in different test methods agreed with one another and provided an internally consistent description of the elastic properties of both a fcc single crystal and a polycrystalline Lennard-Jones material. Because the Lennard-Jones solid satisfies the Cauchy relationships, only two elastic constants are needed to represent the cubic single-crystal behavior and only one independent elastic constant, the bulk modulus, is needed to describe the isotropic elastic properties. It was found that the temperature dependence of the bulk moduli is generally consistent with the thermodynamic requirement that moduli approach absolute zero with zero slope. Lastly, it appears that molecular-dynamics simulation at very low temperatures has a tendency to overestimate the elastic stiffnesses because the atoms do not move fast enough to maintain an equilibrium structure.

ACKNOWLEDGMENTS

The authors take this opportunity to thank Dr. J. Maher, Dr. M. Marcus, and Dr. R. J. Sladek for their useful comments. D.J.Q. expresses gratitude to Eastman Kodak Company for their support.

- ¹L. M. Holtzman, J. B. Adams, S. M. Foiles, and W. N. G. Hitchon, *J. Mater. Res.* **6**, 298 (1991).
- ²F. Milstein and J. Marschall, *Acta. Metall. Mater.* **40**, 1229 (1992).
- ³F. Milstein and A. M. Budek, *Z. Naturforsch.* **42a**, 889 (1987).
- ⁴C. L. Bryant and J. J. Burton, *J. Chem. Phys.* **63**, 2045 (1975).
- ⁵A. Rahman, *Phys. Rev. A* **136**, 405 (1964).
- ⁶L. Verlet, *Phys. Rev.* **159**, 98 (1967).
- ⁷J. P. Bareman, G. Cardini, and M. L. Klein, *Phys. Rev. Lett.* **60**, 2152 (1988).
- ⁸D. W. Noid, G. A. Pfeffer, S. Z. D. Cheng, and B. Wunderlich, *Macromolecules* **21**, 3482 (1988).
- ⁹J. A. Mann, G. J. Tjatjopoulos, M.-O.J. Azzam, K. E. Boggs, K. M. Robinson, and J. N. Sanders, *Thin Solid Films* **152**, 29 (1987).
- ¹⁰S. Wu, *Polymer Interface and Adhesion* (Dekker, New York, 1982).
- ¹¹B. W. Davis, *J. Colloid Interface Sci.* **59**, 420 (1977).
- ¹²G. Simmons and H. Wang, *Single-Crystal Elastic Constants and Calculated Aggregate Properties: A Handbook*, 2nd ed. (M.I.T., Cambridge, MA, 1971).
- ¹³*Thermophysical Properties of Matter*, edited by Y. S. Touloukian, The TPRC Data Series, Vols. 1–13 (Plenum, New York, 1970).
- ¹⁴A. Paskin, A. Gohar, and G. J. Dienes, *Phys. Rev. Lett.* **44**, 940 (1980).
- ¹⁵D. J. Quesnel, D. S. Rimai, and L. P. DeMejo (unpublished).
- ¹⁶B. D. Cullity, *Elements of X-ray Diffraction*, 2nd ed. (Addison-Wesley, Reading, MA, 1978), p. 516.
- ¹⁷W. H. Press, B. P. Flannery, S. A. Teukolsky, and W. T. Vetterling, *Numerical Recipes, the Art of Scientific Computing* (Cambridge University, Cambridge, England, 1986).
- ¹⁸J. M. Haile, *Molecular-Dynamics Simulation: Elementary Methods* (Wiley, New York, 1992), p. 158.
- ¹⁹E. P. Cunningham, *Digital Filtering: An Introduction* (Houghton Mifflin, Boston, 1992).
- ²⁰H. B. Huntington, *The Elastic Constants of Crystals* (Academic, New York, 1958).
- ²¹W. Voigt, *Lehrbuch der Krystallophysik* (Teubner, Leipzig, 1928), p. 962.
- ²²A. Reuss, *Z. Angew. Math. Mech.* **9**, 49 (1929).
- ²³R. Hill, *Proc. Phys. Soc. London Sect. A* **65**, 349 (1952).
- ²⁴Z. Hashin and S. Shtrikman, *J. Mech. Phys. Solids* **10**, 335 (1962); **10**, 343 (1962).
- ²⁵F. A. McClintock and A. S. Argon, *Mechanical Behavior of Materials* (Addison-Wesley, Reading, MA, 1966).
- ²⁶S. P. Timoshenko, *History of Strength of Materials* (Dover, New York, 1983).
- ²⁷A. E. H. Love, *A Treatise on the Mathematical Theory of Elasticity*, 4th ed. (Dover, New York, 1944).
- ²⁸G. S. Zhdanov, in *Crystal Physics*, edited and translated by A. F. Brown (Academic, New York, 1965).
- ²⁹S. D. Poisson, *Mem. Acad.* **8**, 357 (1829).
- ³⁰J. F. Nye, *Physical Properties of Crystals* (Clarendon, Oxford, 1986).
- ³¹K. F. Graff, *Wave Motion in Elastic Solids* (Ohio State University Press, Ohio, 1975).
- ³²F. R. Shanley, *Strength of Materials* (McGraw-Hill, New York, 1957).
- ³³D. J. Quesnel, D. S. Rimai, and L. P. DeMejo, *Solid State Commun.* **85**, 171 (1993).
- ³⁴L. C. Thomas, *Fundamentals of Heat Transfer* (Prentice-Hall, Englewood Cliffs, NJ, 1980).
- ³⁵S. Nose and F. Yonezawa, *J. Chem. Phys.* **84**, 1803 (1986).
- ³⁶M. Gsanger, H. Egger, and E. Lusscher, *Phys. Lett.* **27A**, 695 (1968).
- ³⁷W. D. Callister, *Materials Science and Engineering: An Introduction* (Wiley, New York, 1985).